Strengthening of ods silver wires

Wasserbäch, W.; Skrotzki, W.; Chekhonin, P.;

Originally published:

July 2020

Materialia 12(2020), 100818

DOI: https://doi.org/10.1016/j.mtla.2020.100818

Perma-Link to Publication Repository of HZDR:

https://www.hzdr.de/publications/Publ-31397

Strengthening of ODS Silver Wires

Werner Wasserbäch[a, *], Werner Skrotzki[b, **] and Paul Chekhonin[c]

[a] Institute for Materials Science, University of Stuttgart, 70569 Stuttgart, Germany,

[b] Institute of Solid State and Materials Physics, Dresden University of Technology, 01062 Dresden, Germany

[c] Helmholtz-Zentrum Dresden-Rossendorf e.V., Institute of Resource Ecology, Structural Materials Department, 01328 Dresden, Germany

***** Corresponding author. E-Mail: werner.wasserbaech@imw.uni-stuttgart.de

** Corresponding author. E-Mail: werner.skrotzki@tu-dresden.de

Keywords: Silver, Metal matrix composites, Cold-working, Strain hardening, Texture

Abstract

The present work is part of an experimental programme in which the mechanical behavior and the evolution of microstructure and texture of different industrially manufactured oxide-dispersion strengthened silver alloys upon different processing steps like hot-extrusion, cold-working and further annealing have been investigated. The investigations reveal that the incoherent oxide particles strongly influence the evolution of microstructure and texture during processing and consequently the deformation behavior at room temperature. Small oxide particles cause a high strengthening of the material but only a small change of the microstructure and texture. Increasing the oxide particle size subsequently reduces the strength and changes the original microstructure and texture in a more pronounced way. The yield strength at room temperature can be explained with a linear superposition of the Orowan stress for bypassing of oxide particles by dislocations and grain boundary strengthening according to Hall-Petch. The impact of texture of the materials on the yield strength is accounted for.

1. Introduction

Metal matrix composites are important structural materials used in industrial applications as well as in daily life. A main requirement on their properties is resistance against failure, especially under the influence of mechanical load. Hence, a thorough understanding of their deformation behavior (stress-strain-curves, strain-hardening, hardness, fracture, etc.) is an essential precondition for the selection of suitable materials for industrial processing. An improvement of the mechanical strength is achieved, for example, by a combination of grain boundary strengthening according to Hall [1] and Petch [2] with obstacle strengthening of a second phase according to Orowan [3, 4]. In the case of silver-based electrical contact materials the silver matrix is hardened by the addition of incoherent and insoluble oxide particles such as, for example, tin oxide. After hot-extrusion of the oxide-dispersion strengthened (ODS) starting material the further processing steps are wire-drawing

and cold-heading for rivet production. Hence, a thorough knowledge of the microstructure and the mechanical properties of each material state is an absolute requirement prior to further processing. It is the aim of the present paper to study the influence of oxide particles, silver grain size and texture on the mechanical behavior at room temperature (RT) of the ODS silver materials. Particular attention is paid to the evolution of the microstructure and texture upon cold-working.

2. Experimental

2.1 Mechanical investigations

The production of the ODS silver alloys investigated follows industrial processes, namely internal oxidation (IO materials) and standard powder metallurgy (PM materials). The alloy compositions were designed to yield a total oxide content of 8, 12 and 14 wt.%. Accordingly, in the following the materials are denoted as IO8, IO12, IO14 and PM12. Details of the manufacturing methods are described in [5]. In order to study the RT mechanical behavior of the materials, tensile samples of 100 mm length were cut from hot-extruded rods and in the case of the IO14 material after different steps of wire-drawing and annealing. The wire-drawing speed was about 30 m/min, which corresponds to a nominal strain rate of about 100 s^{-1} (see, for example Dieter [6]). The strain of each wire-drawing step was about 20%, the final wire diameter was about 1.4 mm. The wire-drawn samples after each drawing step have been annealed for 2 h at 600°C in order to improve their ductility before further wire-processing. All IO and PM materials were deformed in tension at RT until fracture using an Instron testing machine operating at a constant cross-head speed of 3 mm/min yielding a nominal initial axial strain rate of 5×10^{-4} s^{-1}. The parabolic type stress - strain (σ - ε) curves have been analyzed with regard to the mechanical parameters yield strength (σ_y) at 0.2% plastic strain, nominal fracture strain (A_{100}) and strain-hardening coefficient ($d\sigma/d\varepsilon$).

2.2 Microstructure and texture evaluation

The microstructures and textures of the materials were analyzed by scanning electron microscopy (SEM), electron backscatter diffraction (EBSD) and X-ray diffraction (XRD). A detailed description of the sample preparation procedure is given in [5]. The microstructure was evaluated by the EBSD technique (see, for example Engler and Randle [7]). A Zeiss LEO438VP SEM microscope operating at 20 kV equipped with a TSL/EDAX EBSD system (Draper, UT 84020, USA) was used. The EBSD data were further analyzed with the software program TSLOIM 5.0 (also Draper, UT 84020, USA). The grain size is taken as diameter of an area equivalent circle. Grains are defined by grain boundaries with a misorientation >10° (high angle grain boundaries, HAGBs). The texture was measured with a texture goniometer (Bruker AXS D8 Discover, Karlsruhe, Germany) using Cu K_α X-ray radiation with a beam diameter of 2 mm. From the measured pole figures (200, 220, 111) the orientation distribution function (ODF) is calculated using the software programs

TexEval (also Bruker, Karlsruhe, Germany) and MTEX 3.2 (Hielscher and Schaeben [8]). In general, the texture of face-centered cubic (fcc) metals after axisymmetric deformation, such as extrusion, wire-drawing or tensile deformation, consists of a <001> <111> double fiber texture (see, for example, Wassermann and Grewen [9]). This type of texture is best represented as inverse pole figure (IPF) recalculated from the ODF. The volume fractions V of the <100> and <111> fibers have been calculated from the ODFs according to Hosford et al. [10]. A “texture sharpness” value (texture index) according to Bunge [11] to describe the strength of the fiber textures was calculated with MTEX 3.2 [9].

3. Results

3.1 Deformation behavior

In Fig. 1 the RT true stress - true strain curves of the as-extruded ODS silver alloys and of a commercially pure (99.97%) silver wire (diameter 3 mm and additionally annealed for 2 h at 600°C in a protective atmosphere prior to testing) are shown. All specimens exhibit a parabolic stress - strain curve typical for polycrystalline materials, and a substantial amount of ductility, i.e. the nominal fracture strains A_{100} are of the order of 20% to 30%. The most prominent features of the flow stress curves are their high stress level and their high initial strain-hardening as compared with the pure silver wire. It is obvious, that this increase in stress level and high initial work-hardening has to be attributed to the microstructure and the texture of the ODS silver alloys.

In Fig. 2 the work-hardening curves $d\sigma/d\varepsilon$ are plotted against the flow stress $\sigma - \sigma_y$. The strain-hardening rate $d\sigma/d\varepsilon$ as a function of stress has been numerically computed from the measured stress - strain curves. The strain-hardening curves of all ODS silver alloys exhibit two different stages: one with a steadily decreasing strain-hardening rate and another with an almost constant one. This behavior is typical for high stacking fault energy (SFE) polycrystalline fcc alloys (i.e. stage III and stage IV according to Argon and Haasen [12]). However, a four-stage behavior typical for low SFE metals, such as 70:30 brass with a SFE similar to silver, proposed by Asgari et al. [13] could not be observed. Figure 2 shows that the materials with small oxide particles (Tab. 1) have the highest initial work-hardening rates. The high work-hardening only occurs at low true strains ($\varepsilon < 2\%$).

In Tab. 1 the main mechanical properties as yield strength σ_y, nominal fracture strain A_{100}, and initial strain-hardening coefficient θ_0 are summarized with the main microstructural parameters oxide particle volume fraction f, mean oxide particle size (median value of the particle size number fraction taken at a cumulative frequency of 50%) d_{50}, oxide particle spacing λ and mean silver grain size (median value of the grain size area fraction taken at a cumulative frequency of 50%) D_{50}. The oxide particle size d_{50} and the silver grain size D_{50} are averaged over cross and longitudinal section of the samples. It should be mentioned that the grain size given in [5] for some of the materials used here is smaller because low angle grain boundaries

(LAGBs) were included. The oxide particle spacing λ (mean free path) has been calculated with Fullman's expression [14]

$$\lambda \approx 2\,(1 - f)\,d_{50}/3f. \qquad (2)$$

From the results in Tab. 1 it is obvious that compared to pure silver the addition of oxide particles increases the yield strength σ_y and the initial work-hardening rate θ_0.

Table 1: Oxide particle volume fraction f, oxide particle diameter d_{50}, oxide particle separation λ, silver grain size diameter D_{50}, yield strength σ_y, fracture strain A_{100}, and initial strain-hardening coefficient θ_0 of the hot-extruded ODS materials and an Ag 99.97 wire.

Material	IO8	IO12	IO14	PM12-1	PM12-2	PM12-3	Ag 99.97
f (*)	0.12	0.16	0.20	0.17	0.17	0.17	---
d_{50} [µm]	0.16 ± 0.02	0.20 ± 0.03	0.22 ± 0.04	0.36 ± 0.07	0.56 ± 0.16	0.93 ± 0.20	---
λ [µm]	0.78 ± 0.1	0.70 ± 0.1	0.59 ± 0.1	1.17 ± 0.2	1.82 ± 0.5	3.03 ± 0.7	---
D_{50} [µm]	7.22 ± 1.1	3.35 ± 0.5	2.72 ± 0.3	3.54 ± 0.5	4.43 ± 0.5	5.00 ± 0.5	---
σ_y [MPa]	142 ± 4	166 ± 4	182 ± 5	136 ± 4	118 ± 5	106 ± 4	43 ± 3
A_{100} (*) [%]	15	33	20	29	30	29	30
θ_0 (**) [GPa]	14	16	19	13	8	7	2

(*) The errors in f and A_{100} are less than 1%.

(**) The θ_0 values have been taken from the strain-hardening curves in Fig. 2 at $\sigma - \sigma_y = 0$.

The as-extruded materials are further processed by wire-drawing and cold-heading for rivet production. Therefore, it is of considerable interest to study their microstructure, texture and mechanical behavior after the different production steps. We confine us to the wire-drawing process of the material IO14 during which the diameter Ø was subsequently reduced from 5.5 mm down to 1.4 mm in 14 steps (with a nominal strain step of about 20%). After each wire-drawing step, the samples have been annealed for 2 h at 600°C. The RT true stress – true strain curves of the different wires drawn to diameters of 4 mm (4 deformation steps), 3 mm (8 deformation steps), 2 mm (11 deformation steps) and 1.4 mm (14 deformation steps) are shown in Fig. 3 together with that of the as-extruded material (Ø = 5.5 mm). All

specimens exhibit a parabolic stress - strain curve and a substantial amount of ductility. Surprisingly, an increase (as compared to the as-extruded material) of about 15% of the flow stress of the wire-drawn and annealed samples is observed. The strain-hardening rate as a function of stress of the wire-processed materials exhibits only two different stages (see Fig. 4). The grain size D_{50} and mechanical parameters σ_y, A_{100}, and θ_0 of the wires with diameter Ø are summarized in Tab. 2.

Table 2: Diameter Ø, grain size D_{50}, yield strength σ_y, fracture strain A_{100}, and initial strain-hardening coefficient θ_0 of the as-extruded and wire-drawn IO14 material.

Ø [mm]	5.5	4.0	2.9	2.0	1.4
D_{50} [µm]	2.72 ± 0.3	4.54 ± 0.4	4.59 ± 0.4	3.52 ± 0.4	---
σ_y [MPa]	182 ± 5	198 ± 4	200 ± 5	211 ± 4	209 ± 3
A_{100} [%]	20	26	22	30	34
θ_0 (**) [GPa]	19	18	18	18	19

(*) The errors in A_{100} are less than 1%

(**) The θ_0 values have been taken from the strain-hardening curves in Fig. 4 at $\sigma - \sigma_y = 0$.

During wire-drawing fracture of the oxide particles may have taken place (see, for example Bergmann and Wassermann [15]) and/or oxide particle coarsening during annealing (see, for example Groza and Gibeling [16]). To check this, the oxide particle distribution and oxide particle size of each IO14 wire was analyzed by backscatter electron imaging. After all wire-drawing steps down to a diameter of 1.4 mm, the oxide particle distribution is rather homogeneous and the oxide particle size exhibits a typical lognormal distribution similar to that in the as-extruded alloy (see Figs. 1 and 2 in [5]). The investigations reveal that the oxide particle distributions in the wire samples keep almost unchanged during the different wire-drawing and annealing steps. Especially, the mean oxide particle size diameter d_{50} averaged over cross and longitudinal section remained unchanged within the experimental errors. Hence, it must be concluded that the observed increase of σ_y of the drawn and annealed wires has to be attributed to a change in the microstructure and texture of the silver matrix (see next section 3.2).

3.2 Microstructure and texture before deformation

A detailed characterization of the microstructure and texture of the as-extruded IO and PM materials is outlined in [5]. A main result is, that in all alloys, <100> fiber

textures parallel to the extrusion direction were observed. The microstructure and the texture sharpness strongly depend on the spacing of the oxide particles. With increasing spacing of the oxide particles, the silver grain size and the fraction of $\Sigma 3$ annealing twins increases and the texture sharpness decreases. In Fig. 5 the microstructures and textures of the as-extruded materials IO14 and PM12-3 are shown together with that of material IO14 after 11 drawing and annealing steps. Figs. 5a and b and 5d and e show as examples the microstructure and texture of the as-extruded materials IO14 and PM12-3. After subsequent wire-drawing and annealing steps the microstructure and texture of the material IO14 have been significantly changed (Figs. 5g and h). The original sharp <100> texture (fiber intensity of about 22.6) after wire-drawing and annealing has changed to a weak <100> <111> double fiber texture (intensity of both fibers of about 2.0). Similarly, the <100> volume fraction decreased from almost 94% to about 34% after the wire-drawing and annealing steps, whereas the <111> volume fraction increases from almost zero to about 16%. In addition, the original high texture index of 10.74 is reduced to about 1.2 after wire-drawing and annealing, which is close to 1, the value for a random texture (see, Bunge [11]). In the microstructures of the processed wires an increased density of $\Sigma 3$ annealing twins can be observed. These annealing twins seem to randomize the texture (see, for example, Gottstein [17]). Table 3 summarizes the texture parameters of the matertials before tensile deformation (i.e. volume fraction V of the <100> and <111> fiber components, texture index and Taylor factor). The Taylor factor M has been calculated from the respective fiber volume fractions. For example, in the case of the as-extruded material IO14 M is given by $0.94\ M_{<001>} + 0.01\ M_{<111>} + 0.05\ M_{<random>} = 2.49$, where $M_{<100>} = 2.45$, $M_{<111>} = 3.67$ and $M_{<random>} = 3.06$.

Table 3: Texture parameters: volume fractions V <100> and V <111>, texture index and Taylor factor. IO14 ann denotes material IO14 after different wire drawing and annealing steps.The values of IO14 ann are averaged over all wires.

Material	IO8	IO12	IO14	PM12-1	PM12-2	PM12-3	IO14 ann
V <100> [%]	93.8	93.1	93.8	88.6	77.0	67.9	~ 34
V <111> [%]	1.0	1.0	1.0	3.0	6.0	10.0	~ 16
Texture Index	12.50	10.22	10.74	7.36	3.57	2.76	~ 1.20
Taylor factor	2.49	2.49	2.49	2.54	2.63	2.71	~ 2.95

3.3 Microstructure and texture evolution upon cold working

In the case of the IO materials (IO12 and IO14) and the PM material PM12-1 with relatively small oxide particles, the texture of the samples exhibits a strong <100> fiber component, which is only weakly reduced during tensile deformation at RT. As an example, Fig. 5c shows the texture of the tensile deformed material IO14. Within the experimental errors, the silver grain size D_{50} of the samples is not changed by RT tensile deformation. However, a remarkable change in the fractions of LAGBs and HAGBs can be observed. Upon tension, the fraction of LAGBs considerably increases, whereas the fraction of HAGBs decreases. The quantitative evaluation of the texture parameters (i.e. fiber volume fraction and texture index) reveals that they are only weakly influenced by the tensile deformation of the samples. Hence, it is assumed that small oxide particles have only a weak influence on the texture evolution during RT tension.

In the case of the two other PM materials PM12-2 and PM12-3 with larger oxide particles the texture of the as-extruded samples is a <100> <111> double fiber texture (Fig. 5e). Compared to IO14 the <100> fiber intensity is lower and there exists a weak <111> fiber. The influence of RT tension on the texture of the material PM12-3 is shown in Fig. 5f. In this case, tension reduces the intensity of the <100> fiber, while that of <111> is increased. Surprisingly, wire-drawing without annealing steps (not shown here) has a more pronounced effect on the microstructure and texture evolution than tensile deformation, although the same strain (about 30%) is applied in both cases. Perhaps, this has to be attributed to the very high strain rate in the case of wire-drawing, which is about a factor 10^5 higher than that in tensile deformation. As in the case of the materials with small oxide particles a significant increase of the amount of LAGBs and a comparable decrease of HAGBs is observed. In all materials, the increase in density of LAGBs during cold-working has to be attributed to an accumulation of dislocations similar as in particle-free metals (for details see Humphreys and Hatherly [18], chpt. 2). Another main result is that upon cold-deformation of the materials PM12-2 and PM12-3 the amount of the original $\Sigma 3$ annealing twins developed during hot-extrusion is drastically reduced (see Fig. 6). Evidently, deformation twinning during tension as expected for low SFE metals (Asgari et al. [13]) does not compensate this loss. However, it may also be that the very thin deformation twin lamellae are not detected by EBSD.

4. Discussion

4.1 Mechanical properties

First, the impact of the microstructure and texture on the RT yield strength σ_y is considered. In polycrystalline materials containing incoherent particles the yield strength σ_y is the result of a simultaneous occurrence of grain boundary strengthening according to Hall [1] and Petch [2] and of particle hardening due to the Orowan mechanism [3, 4]. Hence, the yield strength principally consists of three contributions:

$$\sigma_y = \sigma_0 + \sigma_{HP} + \sigma_{OR} \qquad (3)$$

with σ_y: macroscopic yield stress of the extruded rod, σ_0: intrinsic yield stress of the polycrystalline Ag matrix metal, σ_{HP}: Hall-Petch contribution due to the grain size, and σ_{OR}: Orowan stress due to the oxide particles. Grundmann et al. [19] have shown that a linear superposition of the three components is suitable at least for a silver grain size well above about 0.5 µm. For the further analysis, we follow the method used by Grundmann et al. [19]. In the first step, the particle hardening is considered. For the Orowan stress, σ_{OR}, we adopt the modified result of Kocks [20]:

$$\sigma_{OR} = M\, A\, [\ln(8r_s/b)]^{3/2}\, [\ln(L_p/b)]^{-1/2}\, (L_p - 2r_s)^{-1} \qquad (4)$$

with $r_s = r\ \pi/4$ (r: average particle radius), $L_p = r\ (2\,\pi/3f)^{1/2}$ (average particle separation), b = 0.289 nm: magnitude of the Burgers vector for Ag and M is the Taylor factor, representing the texture of the material. The pre-logarithmic constant A is given by

$$A = 0.9\ Gb/4\,\pi \qquad \text{for edge dislocations} \qquad (5a)$$

and

$$A = 0.9\ Gb/4\,\pi\,(1 - \nu) \qquad \text{for screw dislocations} \qquad (5b).$$

G is the shear modulus and ν the Poisson ratio. If the anisotropy of the material is taken into account, the isotropic constants G and ν have to be replaced by the respective anisotropic ones (see, for example Ashby [21, 22], Hirsch and Humphreys [23]). The anisotropic shear modulus is given by $G = [½c_{44}\ (c_{11} - c_{12})]^{½}$, where the c_{ik} are the second-order elastic constants which are given by Hiki and Granato [24] (G = 26.74 GPa). The anisotropic Poisson ratio ν_a can be calculated according to Chou and Sha [25] (ν_a = 0.45) . The pre-logarithmic factors A in eqns. 5 (a, b) are revealed to be A = 0.55 GPa nm for edge dislocations and A = 1.01 GPa nm for screw dislocations. For comparison with experimental data, the geometric mean of eq. (5) is frequently recommended to be used (see, for example Ashby [21, 22], Hirsch and Humphreys [23] or Nembach [26]).

The Orowan contribution to the yield strength is particularly effective for particles with a size smaller than about 1 µm (see, for example, Miller and Humphreys [27]). As the IO12 and IO14 have the same texture (i.e. the same Taylor factor) and a comparable grain size, it is possible to estimate the order of the prefactor A by plotting their yield strength σ_y (devided by their Taylor factor M = 2.49) as a function of the Orowan parameter $[\ln(8r_s/b)]^{3/2}\, [\ln(L_p/b)]^{-1/2}\, (L_p - 2r_s)^{-1}$ in eqn. (4). The analysis (not shown here) revealed that the slope A in eqn. (4) must be of the order of 1 GPa nm, close to the theoretical value for screw dislocations. The evaluation of experimentally obtained results of Ebeling and Ashby [28] revealed that the yield stress is lying between the “Orowan” stress for edge and screw dislocations

[21, 23]. Moreover, a comparison with the geometrical average value revealed that the experimentally obtained values lie between the geometrical average value (i.e. A = 0.75 GPa nm) and that for screw dislocations [22]. For the further analysis, a mean pre-logarithmic factor A = 0.88 GPa nm will be used.

In the second step, the influence of grain size hardening according to Hall-Petch is considered. The Hall-Petch equation [1, 2] reads:

$$\sigma_{HP} = \alpha_{HP} D^{-1/2} \qquad (6)$$

with D: silver grain size and α_{HP}: Hall-Petch coefficient for random grain orientations. From eqn. (3) we obtain

$$\sigma_y - \sigma_{OR} = \sigma_0 + \sigma_{HP} \qquad (7)$$

For the further analysis, the yield strength σ_y and the Orowan contribution (eqn. 4) of the different materials are devided by the experimentally found Taylor factor M_{ex} (see Tab. 3) and multiplied with the Taylor factor for random grain orientations (i.e. M = 3.06). The values $3.06\ [\sigma_y - \sigma_{OR}] / M_{ex}$ are then plotted against $D^{-1/2}$ and compared in Fig. 7 with values obtained by Aldrich and Armstrong [29]. These authors investigated the grain size dependence of the yield strength of commercially pure silver. Their specimens were recrystallized and, hence, the microstructure also mainly consists of HAGBs, including possible annealing twins. The grain size was determined with the line intercept method on grain boundary etched surfaces. From their measured line intercept length ℓ a mean grain size is obtained as 3/2 ℓ (Fullman [14]). Our results of the “Hall-Petch” stresses using a pre-logarithmic factor A = 0.88, see above, for the Orowan stress coincide well with their values. The dashed red lines in Fig. 7 were calculated with a pre-logarithmic factor A = 1 GPa nm (the value for screw dislocations; lower line) and with a pre-logarithmic factor A = 0.75 GPa nm (the geometric mean of screw and edge dislocations; upper line). They represent lower and upper estimates of $\sigma_0 + \sigma_{HP}$. The dashed blue line represents a linear fit of the data of Aldrich and Armstrong [29] and is given by

$$\sigma_0 + \sigma_{HP} = 24\ \text{MPa} + 1.38\ \text{MPa cm}^{1/2}\ D^{-1/2} \qquad (8).$$

The same relation also holds for Hall-Petch strengthening of our ODS silver materials, although the grain size has been determined in a different way. The calculated Orowan strength (according to eqn. 4) and Hall-Petch strength (according to eqn. 8) are summarized for the different materials in Tab. 4 taking into account their respective textures through their Taylor factors.

Table 4: Calculated Orowan strength and Hall-Petch strength for the different materials. The notations IO14-4, IO14-3 and IO14-2 denote the wire-drawn material

IO14 at diameters of 4 mm, 2.9 mm and 2 mm, respectively. M denotes the Taylor factor of the materials.

Material	IO8	IO12	IO14	IO14-4	IO14-3	IO14-2	PM12-3	PM12-2	PM12-3
M	2.49	2.49	2.49	2.95	2.95	2.95	2.54	2.63	2,71
σ_{OR} [MPa]	81	85	97	115	115	115	55	38	25
$\sigma_0 + \sigma_{HP}$ [MPa]	61	81	88	86	85	94	81	77	76
$\sigma_0 + \sigma_{OR} + \sigma_{HP}$ [MPa]	142	166	185	201	200	209	136	115	101

From our experimental results (see Figs. 1 – 4) it is obvious that the hard oxide particles not only affect the yield stress but also the strain-hardening rate at small strains below about 1% (i.e. the initial strain hardening coefficient θ_0). According to Mecking and Kocks [30], regime III of the work-hardening curve with a steadily decreasing strain-hardening rate with stress consists of a constant work-hardening coefficient (i.e. θ_0) and a dynamic recovery component. We only consider the work-hardening coefficient θ_0 which accounts for any possible obstacles that hinder dislocation motion. The work-hardening coefficient θ_0 of the pure silver wire is about 2 GPa and comparable with that of pure copper with similar grain size (see for example Asgari et al. [13]). In the case of ODS materials the dislocation motion is strongly hindered by the hard oxide particles. For the material IO14 a work-hardening coefficient θ_0 of about 19 GPa is observed (see Tab. 1).

An early attempt to describe the work-hardening of particle containing metals with the Orowan model has been performed by Fisher et al. [31]. The authors assumed that the Orowan loops around the particles exert a back stress which opposes further slip. They found a linear stress - strain curve in the form (see Hirsch and Humphreys [23])

$$\sigma - \sigma_0 = 6\, G\, f^{3/2}\, \varepsilon \qquad (7a)$$

and hence a work-hardening coefficient

$$\theta_0 = 6\, G\, f^{3/2} \qquad (7b).$$

With an effective shear modulus G ≈ 42 GPa (average between geometric mean and the value for screw dislocations) and an oxide volume fraction of f = 0.2 (material IO14) we obtain $\theta_0 \approx 19$ GPa (taking the texture into account) which is close to the

observed value. However, the work-hardening coefficient as given in eqn. (7b) only depends on the volume fraction of the oxides but not on their size and separation.
Hirsch and Humphreys [23] considered the influence of the particle spacing λ and obtained a linear single-crystalline work-hardening rate proportional to the volume fraction and only weakly dependent on λ (see their eqn. 15.17 in [23]). The initial coefficient of the work-hardening is then given by

$$\theta_0 = d\tau/d\Upsilon \approx 0.05\ G \ln(2\lambda/b)\ f/(1-\nu)^{1/2} \qquad (8)$$

In the polycrystalline case, the work-hardening coefficient is given by $\theta_0 = (d\sigma/d\varepsilon) = M^2\ (d\tau/d\Upsilon)$ (see, for example, Kocks and Mecking [32]). With f = 0.2, G = 26,7 GPa, ν ≈ 0.45 (anisotropic case) and ln(d/b) ≈ 8.3 we obtain in the case of material IO14 with M ≈ 2.5 a polycrystalline work-hardening coefficient $\theta_0 \approx 18.6$ GPa.

As shown by Ashby [21, 22 and 33 - 35], the observed single-crystalline work-hardening curves of the dispersion-hardened metals are not linear but roughly parabolic

$$\tau - \tau_0 = \alpha\ G\ (2\ b\ f\ \Upsilon / d)^{1/2}, \qquad (9)$$

with d size of the particles, ϒ shear strain and α constant of the order of 0.25. The single-crystalline work-hardening coefficient θ_0 is then given as the slope of the work-hardening curve at a plastic strain of 0.2% In the case of material IO14 we obtain at the yield point the single-crystalline value $\theta_0 \approx 2.92$ GPa. Hence, a value of about 18 GPa is obtained for the polycrystalline material using M ≈ 2.5. The results as obtained from eqns. (7 - 9) are summarized in Tab. 5.

Table 5: Initial work-hardening coefficients θ_0 as calculated with eqns. (7 - 9).

Material	IO 8	IO 14	IO 12	PM12-1	PM12-2	PM12-3
(FHP*) θ_0 [GPa]	9	19	13	15	15	16
(HH**) θ_0 [GPa]	12	19	15	18	22	22
(Ashby***) θ_0 [GPa]	16	18	17	13	10	8
Measured θ_0 [GPa]	14	19	16	13	8	7

FHP *: Fisher et al. [31]; HH**: Hirsch and Humphreys [26]; Ashby***: [21, 22; 33-35]
Within the experimental errors and the limitations of the theoretical models, the agreement between the calculations according to Ashby [21, 22; 33-35] and the observed initial work-hardening coefficients θ_0 seems to be quite reasonable.

4.2 Microstructure and texture upon cold-working

During the RT tensile deformation the microstructure and texture of the original as-extruded starting materials are modified. Although the influence of dispersions like oxides or other non-deformable particles on the mechanical behavior of fcc metals has been reported in numerous papers, investigations of microstructure and texture development upon tensile deformation are relatively few. Most of them tested tensile samples prepared from rolled sheets taking the tensile direction parallel to the rolling direction (see, for example, Ohtani and Inagaki [36, 37]) and are hence not directly comparable with our axisymmetric tensile experiments. As the strain tensor for tensile deformation is comparable with that for wire-drawing or extrusion (see, for example, Murnaghan [38], Hoffman and Sachs [39], Poudens et al. [40]) it seems reasonable to compare our results with those after wire-drawing or cold-extrusion. In highly cold-drawn wires of Ag a <100> <111> double fiber texture was found with <100> dominating (Schmid and Wassermann [41], Ahlborn and Wassermann [42], English and Chin [43]). However, the predominant <100> fiber textures of hot-extruded Ag are due to recrystallization during or immediately after the hot-extrusion process rather than due to sole deformation processes (for details, see [5]).

Systematic investigations of the influence of a second phase on the texture evolution upon cold-working by wire-drawing have been performed by Wassermann and co-workers [15, 44 – 54] for several fcc metals like aluminum, copper, nickel and α–brass. We only consider the impact of non-deformable oxides like Al_2O_3, MgO and SiO_2 on wire-drawing of these metal-matrix composites. A main result was that the deformation texture of the composite materials strongly depends on size and concentration of the oxide particles. Fine particles with diameters less than about 0.2 µm only weakly disturb the original fiber texture present after hot-extrusion, even after a large area reduction of about 60% which corresponds to a true strain of about 100%. Larger particles significantly disturb the original fiber texture. For very large particle sizes (d > 5 µm) a nearly random texture was observed. TEM investigations revealed that high orientation gradients and dislocation density gradients are created around the larger particles (Grewen and Huber [54]), whereas a nearly random dislocation arrangement is observed in the case of small particles (Brimhall and Huggins [55]) which is a consequence of a more homogeneous deformation (Juul Jensen et al. [56]). These large orientation gradients and dislocation density gradients are assumed to cause the disturbance of the original textures (Humphreys [57]; see also Humphreys and Hatherly [18] chpts. 2 and 3). A similar dependence on the particle size was also observed in the case of cold-extruded Al (SiC) alloys (Poudens et al. [40]). Although our specimens are only tensile-deformed to a true strain of about 20% to 30%, a similar - but only weaker - dependence of the texture on particle size is observed (see Figs. 5c and 5f). The stronger disturbance of the fiber texture in material PM12-2 after wire-drawing compared to that after tensile deformation could be easily explained with a model proposed by Humphreys and Kalu [58]. As the strain rate in the case of wire-drawing is about a factor 10^5 higher than that in tensile deformation, a much higher amount of dislocations will

accumulate at the oxides and hence provide stronger orientation gradients and dislocation density gradients.

A main change after cold-working is the deterioration of the annealing twins originally present after hot-extrusion in the PM materials. However, as further experimental results such as from TEM observations are not yet available, a profound discussion of this feature is not possible. In the case of the material IO14 an increased density of $\Sigma 3$ twins is observed in the microstructures of the processed wires (i.e. after wire drawing and subsequent annealing). The occurrence of these twins has to be attributed to recrystallization effects during annealing rather than to the influence of cold-working.

5. Conclusions

The microstructure, texture and mechanical behaviour of industrially manufactured ODS silver alloys have been investigated after hot-extrusion, wire-drawing including annealing steps and subsequent deformation by tension. Based on the results the following conclusions can be made:

1. The observed yield strength σ_y can be explained by a linear superposition of the Orowan stress necessary to bypass particles by dislocations and the grain boundary strengthening according to Hall and Petch. In addition, our results indicate that the texture of the materials has an impact on the yield strength whereby the textures are determined by annealing twins formed either during hot-extrusion or annealing after wire drawing.

2. The initial work-hardening rate θ_0 is mainly influenced by the Orowan process due to the dispersed oxides.

3. The microstructure and the texture upon cold-working strongly depend on the size of the dispersed oxides. In comparison to fine particles with size of about 0.2 µm larger particles significantly disturb the original microstructure and fiber texture present after hot-extrusion.

Acknowledgements

The authors are indebted to Dr. V. Behrens (DODUCO, Pforzheim) for supplying the ODS Ag materials and to Ms. F. Predel and Dr. E. Bischoff (MPI campus Stuttgart) for technical assistance during part of the experiments.

References

[1] E.O. Hall, The Deformation and ageing of mild steel: III Discussion of results, Proc. Phys. Soc. (London) **B64** (1951) 747 – 753.

[2] N.J. Petch, The cleavage strength of polycrystals, J. Iron Steel Inst. **174** (1953) 25 – 28.

[3] E. Orowan, Classification and Nomenclature of Internal Stresses, Proc. Symp. Internal Stresses in Metals and Alloys, London: The Institute of Metals (1948), 47 – 59.

[4] E. Orowan, Discussion III on Internal Stresses, Proc. Symp. Internal Stresses in Metals and Alloys, London: The Institute of Metals (1948), 451 – 453.

[5] W. Wasserbäch, W. Skrotzki, Microstructure and texture development in oxide-dispersion strengthened silver rods processed by hot-extrusion, Materialia **5** (2019), 100175

[6] G.E. Dieter, Mechanical Metallurgy (McGraw Hill, New York, 1986), Chapt. 19.

[7] O. Engler, V. Randle, Introduction to Texture Analysis, CRC Press, London (2010)

[8] R. Hielscher, H. Schaeben: A novel pole figure inversion method: specification of the MTEX algorithm, J. Appl. Cryst. **42** (2008) 1024 - 1037.

[9] G. Wassermann, J. Grewen, Texturen Metallischer Werkstoffe, Springer-Verlag, Berlin (1962).

[10] W.F. Hosford, J. O'Brien, J. House, R. de Angelis, Use of ODF data to quantitatively describe fiber textures, Advances in X-Ray Analysis **42** (2000) 502–509.

[11] H.J. Bunge, Texture Analysis in Materials Science, Butterworth & Co (1982)..

[12] A.S. Argon, P. Haasen, A new mechanism of work hardening in the late stages of large strain plastic flow in fcc and diamond cubic crystals, Acta metall. **41** (1993) 3289 – 3306.

[13] S. Asgari, E. Del-Danaf, S.R. Kalidindi, R.D. Doherty, Strain hardening regimes and microstructural evolution during large strain compression of low stacking fault energy fcc alloys that form deformation twins, Metall. Trans. **A28** (1997) 1781 - 1795

[14] R.L. Fullman, Measurements of particle sizes in opaque bodies, Trans. Met. Soc. AIME **197** (1953) 447 - 452.

[15] H.W. Bergmann, G. Wassermann, Wirkung des effektiven Teilchenabstandes auf die Eigenschaften von Verbundwerkstoffen, Z. Metallkde. **69**, (1978) 126 – 131.

[16] J.R. Groza, J.C. Gibeling, Principles of particle selection for dispersion-strengthened copper, Mat. Sci. Eng. **A171** (1993) 115 – 125.

[17] G. Gottstein, Annealing texture development by multiple twinning in fcc crystals, Acta Metall. **32** (1984) 1117 – 1138.

[18] F.J. Humphreys, M. Hatherly, Recrystallization and Related Annealing Phenomena, Elsevier, Amsterdam (2004).

[19] U. Grundmann, M. Heilmeier, U. Martin, H. Oettel, L. Schultz, Oxide dispersion-strengthened silver: manufacturing and properties, Z. Metallkde **94**, (2003) 587 – 592.

[20] U.F. Kocks, The theory of an obstacle-controlled yield strength, Mater. Sci. Eng. **27** (1977) 291 – 298.

[21] M.F. Ashby, The theory of the critical shear stress and work hardening of

dispersion-hardened crystals, in Proc. Second Bolton Landing Conference on Oxide Dispersion Strengthening (eds. G.A. Ansell, T.D. Cooper, F.V. Lenel, New York, Gordon and Breach 1968) p. 143 – 205.
[22] M.F. Ashby, On the Orowan stress, in Physics of strength and plasticity (ed. A.S. Argon, MIT press 1969) p. 113 – 131.
[23] P.B. Hirsch, F.J. Humphreys, Plastic deformation of two-phase alloys containing small nondeformable particles, in Physics of strength and plasticity (ed. A.S. Argon, MIT press 1969) p. 189 – 216.
[24] Y. Hiki, A.V. Granato, Anharmonicity in noble metals: Higher order elastic constants, Phys. Rev. **144** (1966) 411 – 419.
[25] Y.T. Chou, G.T. Sha, <110> Dislocations in cubic crystals, J. Appl. Phys. **42** (1971) 2625 – 2631.
[26] E. Nembach, Particle strengthening of metals and alloys, J. Wiley, New York (1997).
[27] W.S. Miller, F.J. Humphreys, Strengthening mechanisms in particulate metal matrix composites, Scripta metall. **25** (1991) 33 – 38.
[28] R. Ebeling, M.F. Ashby, Dispersion hardening of copper single crystals, Phil. Mag. **13** (1966) 805 – 833.
[29] J.W. Aldrich, R.W. Armstrong, The grain size dependence of the yield, flow and fracture stress of commercial pure silver, Metall. Trans. **1** (1970) 2547 – 2550.
[30] H. Mecking, U.F. Kocks, Kinetics of flow and strain-hardening, Acta metall. **29** (1981) 1865 – 1875.
[31] J.C. Fisher, E.W. Hart, R.H. Pry, The hardening of metal crystals by precipitate particles, Acta metall. **1** (1953) 336 – 339.
[32] U.F. Kocks, H. Mecking, Physics and phenomenology of strain hardening: The FCC case, Progress Materials Science **48** (2003) 171 – 273.
[33] M. Ashby, The hardening of metals by non-deforming particles, Z. Metallkde. **55** (1964) 5 – 17.
[34] M.F. Ashby, Work hardening of dispersion-hardened crystals, Phil. Mag. **14** (1966) 1157 – 1178.
[35] M.F. Ashby, The deformation of plastically non-homogeneous materials, Phil. Mag. **21** (1970) 399 – 424.
[36] S. Ohtani, H. Inagaki, Texture development during tensile deformation in Al-Mg Alloys, Met. Sci. Forum **408 – 412** (2002) 1483 – 1488.
[37] S. Ohtani, H. Inagaki, Texture development in Al alloys during tensile testing, Z. Metallkd. **94** (2003) 983 – 992.
[38] F.D. Murnaghan, Finite deformation of an elastic solid, J. Wiley New York (1951).
[39] O. Hoffman, G. Sachs, Introduction to the Theory of Plasticity for Engineers, McGraw-Hill, New York (1953).
[40] A. Poudens, B. Bacroix, T. Bretheau, Influence of microstructures and particle concentrations on the development of extrusion textures in metal matrix composites, Materials Sc. Eng. **A196** (1995) 219 – 228.
[41] E. Schmid, G. Wassermann, Über die Textur hartgezogener Drähte, Z. Phys. **42** (1927) 779 - 794.
[42] H. Ahlborn, G. Wassermann, Einfluss von Verformungsgrad und –temperatur auf die Textur von Silberdrähten, Z. Metallkde. **54** (1963) 1 – 6.
[43] T. English, G.Y. Chin, On the variation of wire texture with stacking fault energy in fcc metals and alloys, Acta Metall. 13 (1965) 1013 - 1016.

[44] D. Merz, G. Wassermann, Bildung von Verformungstexturen in heterogenen Legierungen, Z. Metallkde. **56** (1965) 516 - 522.
[45] C. Liesner, G. Wassermann, Influence of dispersed α–Al_2O_3 on the deformation - and recrystallization -texture of copper wires, in Texture in Research and Practice (ed. J. Grewen, G. Wassermann, Springer Verlag, Berlin 1969) 357 – 360.
[46] C. Liesner, G. Wassermann, Verformungsverhalten und mechanische Eigenschaften von Verbundwerkstoffen aus Kupfer mit α-Korund, Z. Metallkde. **69** (1969) 827 – 835.
[47] R. Neuss, G. Wassermann, Verformungsverhalten von Verbundwerkstoffen mit nichtmetallischen anorganischen Zusätzen, Z. Metallkde. **64** (1973) 696 – 704.
[48] G. Wassermann, Deformation mechanism and properties of two phase composite wires, Z. Metallkde. **64** (1973) 844 – 848.
[49] G. Wassermann, Verhalten und Eigenschaften hochverformter Verbund-Werkstoffe mit metallischer Matrix, J. Materials Technology **7** (1976) 125 – 128.
[50] H.W. Bergmann, Mechanische Eigenschaften und Verformungsverhalten einer metallischen Matrix mit nichtmetallischen anorganischen Zusätzen, J. Materials Technology **7** (1976) 129 – 135.
[51] G. Wassermann, H.W. Bergmann, C. Frommeyer, Deformation textures in two-phase systems, in Proc. ICOTOM 5 Vol. I (ed. G. Gottstein, K. Lücke, Springer Verlag, Berlin 1978) 37 – 46.
[52] H.W. Bergmann, C. Frommeyer, G. Wassermann, The dependence of the texture and microstructure in two phase composites on the yield stress of the components, in Proc. ICOTOM 5 Vol. I (ed. G. Gottstein, K. Lücke, Springer Verlag, Berlin 1978) 371 – 377.
[53] H.W. Bergmann. G. Wassermann, Einfluss von unverformbaren Teilchen auf die Strangpresstexturen von Verbundwerkstoffen, J. Materials Technology **12** (1981) 88 – 90.
[54] J. Grewen, J. Huber, Das Entfestigungsverhalten von stranggepressten und nachgezogenen AlMgSi1-Stangen, Z. Metallkde. **68** (1977) 647 – 653.
[55] J.L. Brimhall, R.A. Huggins, Electron-microscopic observations of deformed internally oxidized alloys, Trans AIME **233** (1965) 1076 – 1084.
[56] D. Juul Jensen, N. Hansen, F.J. Humphreys, Effect of metallurgical parameters on the textural development in fcc metals and alloys, in Proc. ICOTOM 8 (ed. J.S. Kallend, G. Gottstein, The Metallurgical Society, Warrendale, 1988) 431 – 444.
[57] F.J. Humphreys, Local lattice rotations at second phase particles in deformed metals, Acta metall. **27** (1979) 1801 – 1814.
[58] F.J. Humphreys, P.N. Kalu, Dislocation-particle interactions during high temperature deformation of two-phase aluminum alloys, Acta metall. **35** (1987) 2815 – 2829.

Figures

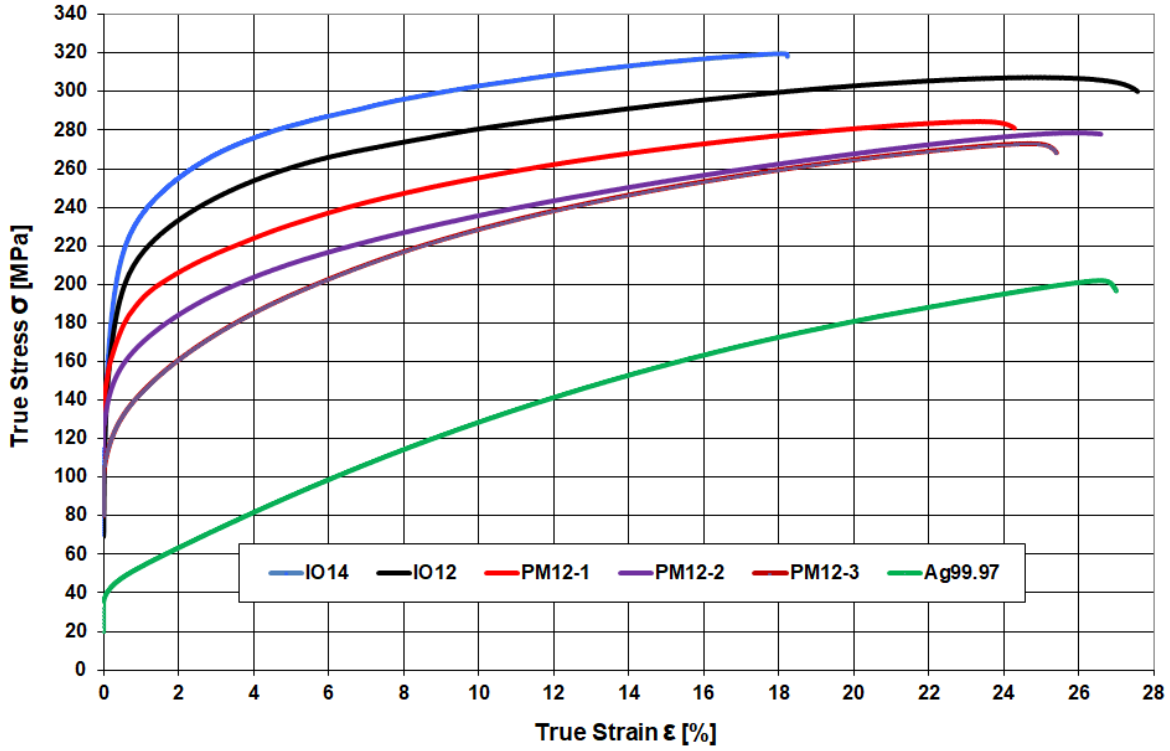

Fig.1: Stress-strain curves of the as-extruded ODS silver alloys together with a pure Ag99.97 wire sample.

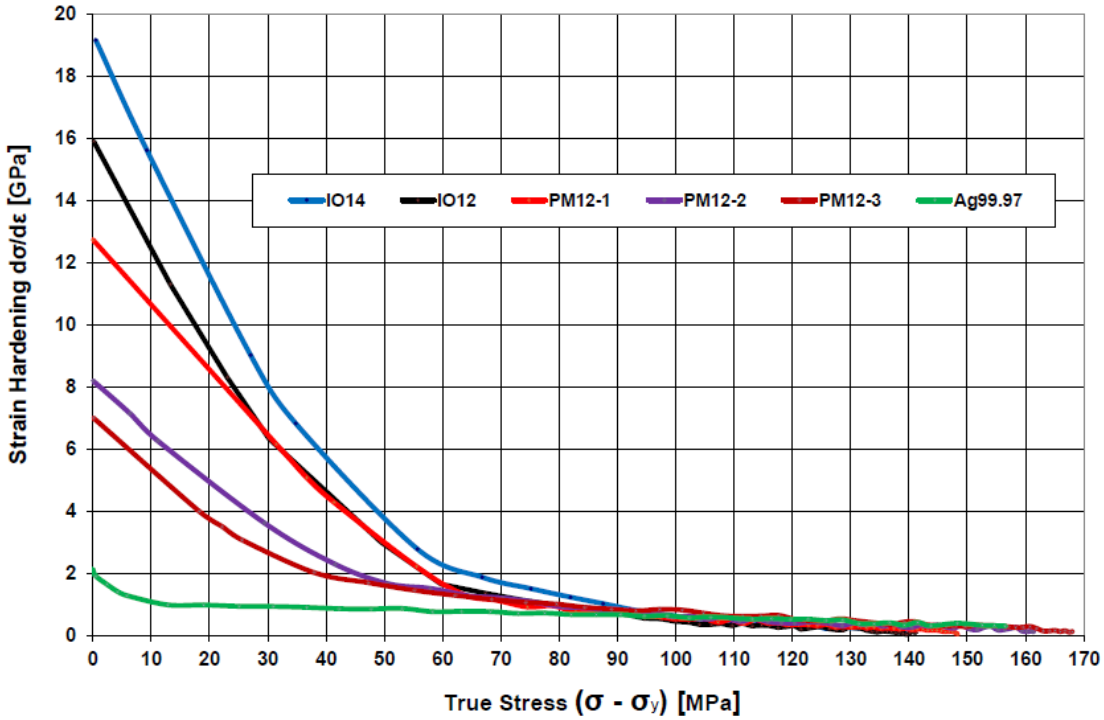

Fig.2: Dependence of the strain-hardening of the as-extruded ODS silver alloys together with a pure Ag99.97 wire sample on the true flow stress ($\sigma - \sigma_y$).

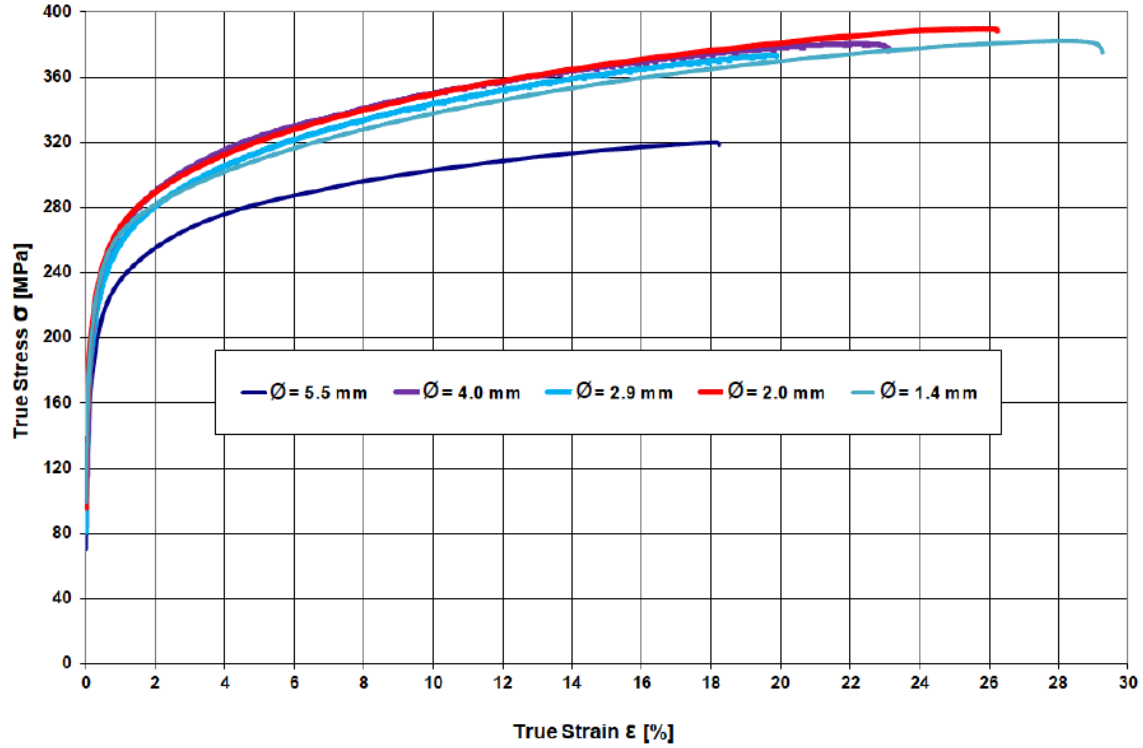

Fig.3: Stress-strain curves of material IO14 after different steps of wire-drawing (Ø = wire diameter) and annealing 2 h at 600°C

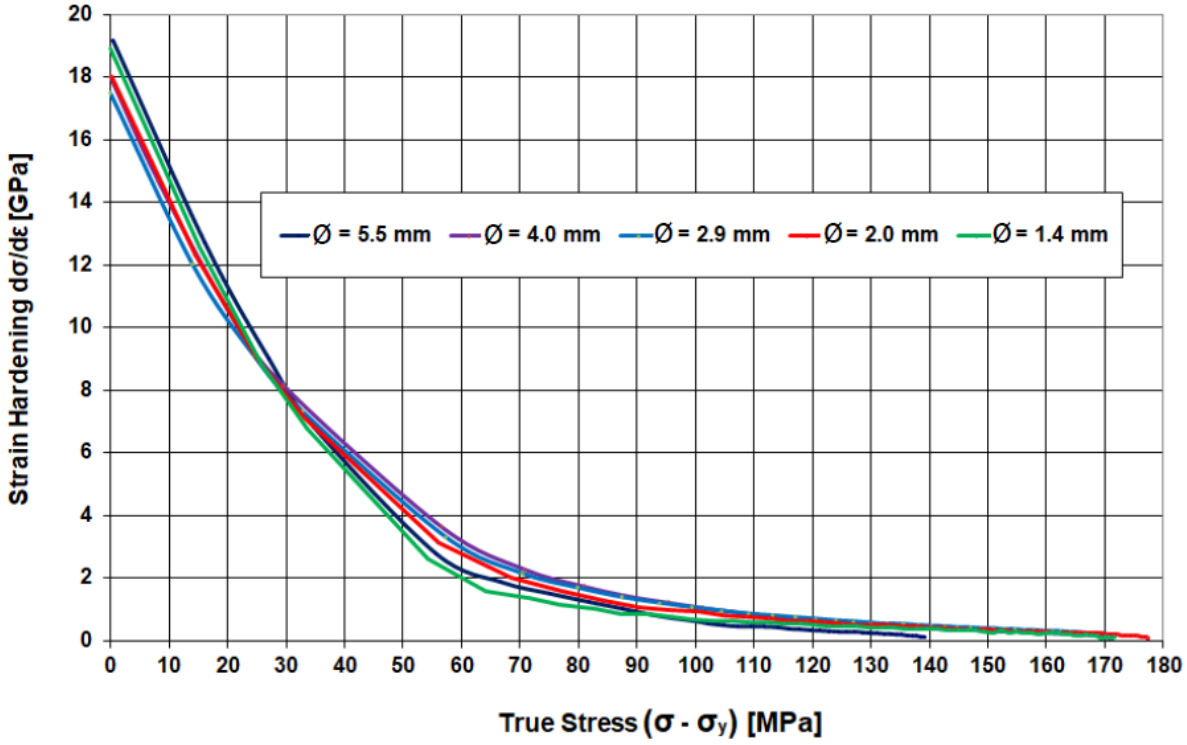

Fig.4: Dependence of the strain-hardening curves of material IO14 after different steps of wire-drawing (Ø = wire diameter) and annealing 2 h at 600°C on the true stress ($\sigma - \sigma_y$).

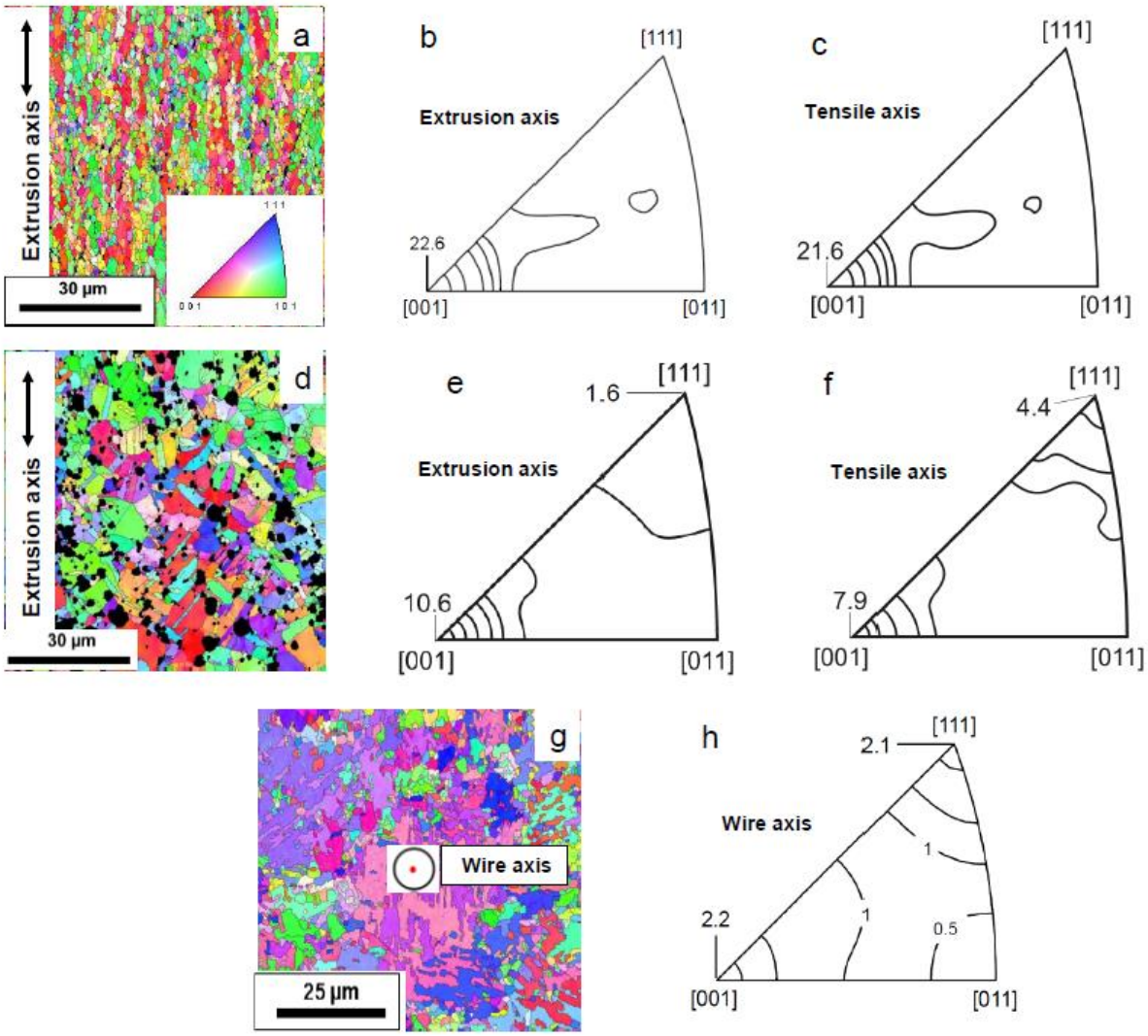

Fig. 5: Microstructure and texture of the materials IO14 and PM12-3:
(a - c) OIM map of a longitudinal section of the as-extruded material IO14 The color code (inset in a) corresponds to the radial direction of the extruded rods. IPF of the as-extruded rod with intensities given in multiples of a random distribution (mrd) (Contour levels 1, 2, 3, 5, 10, 15, max. 22.6); IPF after tensile deformation (Contour levels 1, 2, 3, 5, 10, 15, max. 21.6)
(d - f) OIM map of a longitudinal section of the as-extruded material PM12-3. IPF of the as-extruded rod (Contour levels 1, 2, 3, 5, 7, 9, max. 10.6). IPF after tensile deformation (Contour levels 1, 2, 4, 5, 6 max 7.9).
(g, h) OIM map of a cross section of the material IO 14 after 11 drawing and annealing steps and corresponding IPF (Contour levels 0.5, 1, 1.5, 2 max 2.2).

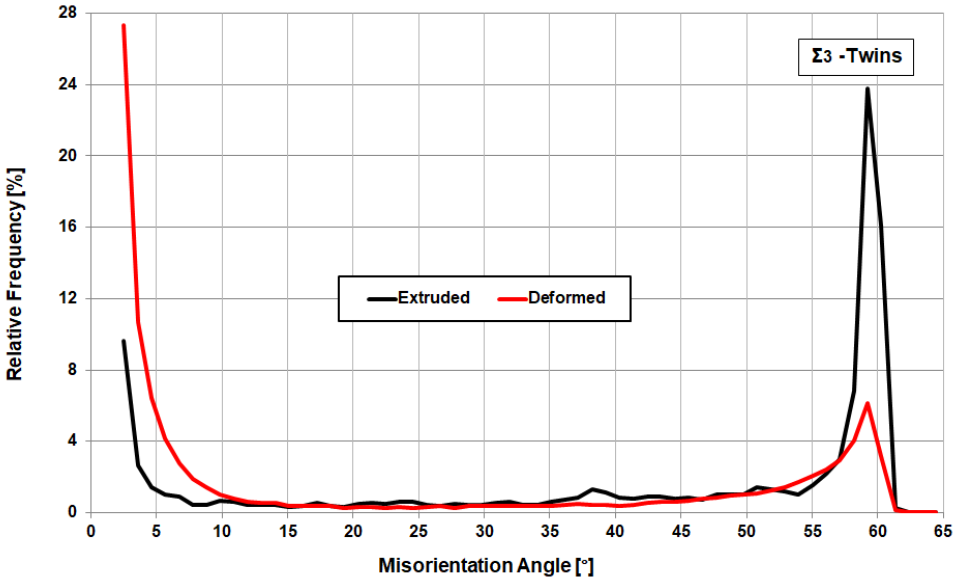

Fig. 6: Misorientation distribution of grains of material PM12-3 before and after tensile deformation

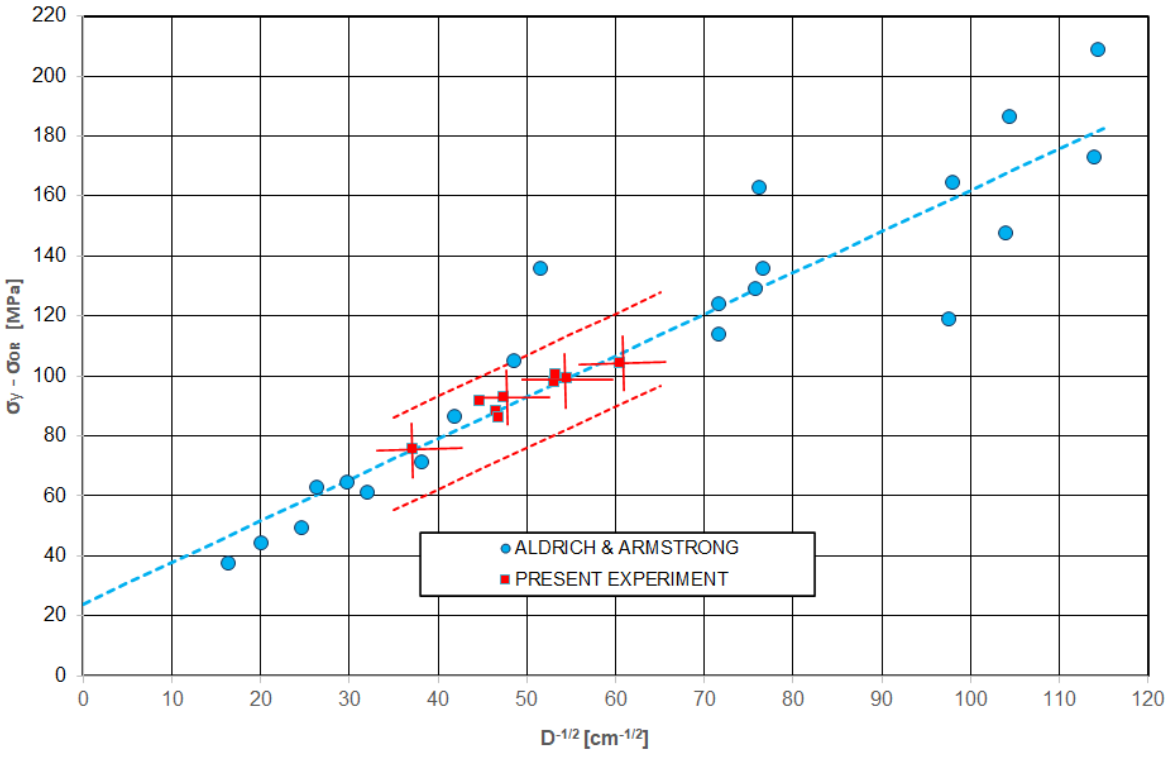

Fig. 7: Hall-Petch contribution to the yield stress of the ODS Ag alloys (red squares) in comparison with the values of commercial purity silver (blue circles) as a function of the inverse square root of the grain size. The values of Aldrich & Armstrong (blue) have been taken from Fig. 2 in their paper [29], taking into account that from their measured line intercept length ℓ a mean grain size D is obtained as 3/2 ℓ [14]. The dashed blue line is the least squares fit of their data. The dashed red lines are calculated for different pre-logarithmic factors A of the Orowan strength (for details see text).